Acta Geotechnica
https://doi.org/10.1007/s11440-026-02972-0

RESEARCH PAPER

Wetting via water condensation of hydrophobic grain surfaces as viewed by synchrotron-radiation computed tomography

Clara M. Toffoli[1] · Marius Milatz [2] · Julian P. Moosmann [3] · Thomas Jentschke [3] · Francisco Williams-Riquer [1] · Felix Beckmann [3] · Jürgen Grabe[1]

Received: 20 February 2025 / Accepted: 5 February 2026

Abstract
The wetting of hydrophobic material via water droplet condensations by means of electronic microscopy and synchrotron computed tomography is investigated in this paper in order to better understand the mechanisms controlling the interaction of hydrophobic granular media and water. In literature so far the behavior has been investigated only by 2D means. In this study, sand and glass beads with similar grain size distribution were made hydrophobic via PFA-C6 cold plasma polymerization. A miniature cooling device based on the Peltier effect for in situ synchrotron computed tomography experiments controlled by a Raspberry Pi was designed and used to induce droplet condensation on the material's surface during CT scanning. The tomograms allow to count droplets and measure their contact angles. Results show that the condensation of those small droplets feature contact angles usually greater than 90° at the beginning of the process, but as time advances, those droplets coalesce, increasing in volume and decreasing in quantity, while their contact angles get progressively smaller. Although hydrophobic behavior and convex menisci were expected in the pendular and funicular regimes, the contact angles of these water structures were closer to 60° at this phase, indicating hydrophilic tendencies. Similarly to wetting via water inflow, the hydrophobicity is lost after a specific degree of local saturation. Unfortunately, the results gathered in this study point in an unfavorable direction for the applications of the hydrophobization technique used here in the macroscale, given their low efficiency in repelling water after reaching the funicular state of the unsaturated regimen and the current discussions about their environmental implications.

Keywords Condensation · Hydrophobic soils · Synchrotron computed tomography

1 Introduction

Research on hydrophobic materials and soils in particular has been conducted for more than a century [11]. In civil engineering, hydrophobic soils have attracted attention because of their potential to act as water-resistant barriers. Typical applications include cover layers for tailings reservoirs during mine closure [5], base, and subbase layers of pavements where repeated wetting and drying cycles can lead to erosion [24] and slope stabilization, where water infiltration may increase the unit weight of the soil and reduce effective stress, potentially triggering failure [23, 26, 27, 54]. In mining engineering, modifying the wettability of soils can also enhance material processing efficiency [7].

Hydrophobicity is commonly characterized by the contact angle (CA), which is defined by the balance of surface tensions at the three-phase contact line where solid, liquid, and gas phases meet. A material is considered water repellent when the contact angle exceeds 90°, and wettable otherwise [26]. The sessile drop method is typically used to measure this angle using a goniometer [2]. In this method, a microscope captures an image of a water droplet immediately after it is placed on the surface of the material, allowing the contact angle to be determined. For granular

✉ Clara M. Toffoli
clara.toffoli@tuhh.de

[1] Institute of Geotechnics and Construction Management, Hamburg University of Technology, Hamburg, Germany

[2] Institute of Geomechanics und Geotechnics, Braunschweig University of Technology, Braunschweig, Germany

[3] Helmholtz-Zentrum Hereon, Geesthacht, Germany

Published online: 21 April 2026

materials, the test is commonly performed by attaching a single-grain layer to a glass plate before placing the droplet. In addition to contact angle measurements, several other methods are used to assess hydrophobicity at different scales and persistence levels, including the water droplet penetration time (WDPT) test, the ethanol molarity test, the capillary rise method, and the Wilhelmy plate method [12, 16, 21, 47, 48].

An illustration of hydrophobic behavior is shown in Fig. 1, where artificially colored water droplets rest on the surface of hydrophobic sand. Food dye was added to the water to enhance visual contrast.

Beyond macroscopic descriptions, several studies have applied particle-scale micromechanical frameworks to investigate the behavior of hydrophobic soils. These studies suggest that suction (ΔP) in unsaturated hydrophobic materials may become positive [5, 17, 18, 22]. This is attributed to the formation of convex menisci between particles, which, by definition, exhibit contact angles greater than 90°. According to the Young–Laplace equation (1), a convex meniscus corresponds to a positive mean radius of curvature ($\bar{r}$), implying that the liquid pressure inside the meniscus (P_{in}) exceeds the gas pressure outside (P_{out}). Here, γ_{lv} denotes the surface tension at the liquid–gas interface.

$$\Delta P = P_{in} - P_{out} = \gamma_{lv} \cdot \frac{1}{\bar{r}} \tag{1}$$

Under these conditions, a repulsive force may act on the surrounding particles, potentially increasing interparticle spacing. The net force results from the balance between suction forces (F_s) and surface tension forces (F_{st}), and repulsion occurs only when the magnitude of the negative suction force exceeds that of the surface tension force [25].

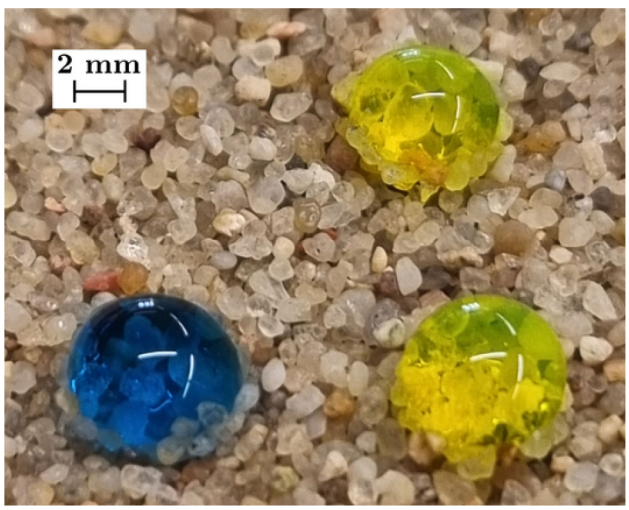

Fig. 1 Artificially colored droplets resting on a hydrophobic sand surface

In fact, convex menisci have been observed in hydrophobic soils using two-dimensional imaging techniques, particularly electron microscopy [5, 17, 18, 25]. However, despite this microscale evidence, the literature reports no strong indication of positive pore water pressure at the macroscale [9].

In contrast to these observations, preliminary investigations conducted by the authors [45], which motivated the synchrotron proposal underlying the present study, revealed that menisci formed between grains via water-vapor condensation often exhibit contact angles smaller than 90°. This indicates that, beyond a certain degree of saturation, the system behaves effectively as hydrophilic. The objective of this paper is therefore to improve the understanding of this wetting mechanism and to identify the processes responsible for the apparent loss of hydrophobicity, despite the existing evidence of convex menisci that could induce repulsive interparticle forces. Specifically, the wetting of hydrophobic granular materials through water-vapor condensation is investigated.

Previous studies on hydrophobic soils have mainly focused on wetting through liquid water imbibition or drying through drainage [4, 8, 9, 49]. These studies consistently show that wettability increases with increasing water content, implying a gradual loss of hydrophobicity as the material interacts with water. In some other cases, this loss has been attributed to the breakdown of hydrophobic coatings associated with plant-derived oils or extreme drying. Those mechanisms are however not the focus of the present work. Detailed investigations of wetting induced by water-vapor condensation, particularly using three-dimensional imaging techniques, remain scarce. To the authors' knowledge, existing studies are limited to analyses based on two-dimensional imaging [18, 25, 45]. Importantly, wetting through vapor condensation can differ significantly from wetting by direct liquid deposition, even though both processes involve similar physical mechanisms such as surface tension, fluid pressure, contact angle hysteresis, and gravity. These differences can lead to markedly different wetting behaviors and contact angles [31, 35]. Comparable investigations on wettable materials using synchrotron imaging to study evaporation and condensation of menisci have been reported by [38].

To address these gaps, the present study employs high-resolution two- and three-dimensional imaging techniques, namely environmental scanning electron microscopy (ESEM) and synchrotron computed tomography (CT), to investigate wetting processes at the microscale. These methods provide sufficient spatial resolution to resolve individual grains and their associated water structures. A miniaturized in situ cooling device capable of inducing water-vapor condensation was developed and deployed at the High Energy Materials Science (HEMS) Beamline P07

at PETRA III, operated by the Deutsches Elektronen-Synchrotron (DESY) in Hamburg, Germany. This setup enabled controlled condensation of water droplets on the surface of hydrophobic granular materials, with droplet growth captured over time. The resulting sequential three-dimensional datasets allow quantification of droplet formation, temporal evolution of contact angles, and subsequent development of menisci and water clusters within the granular assembly.

2 Materials and methods

2.1 Granular materials and their hydrophobic coating

Hamburg Sand, a model sand frequently used at Hamburg University of Technology, and soda-lime glass beads with an equivalent grain size distribution were used in this study. Figure 2 presents their similar grain size distribution. The reason for using two different types of material is to observe the influence of angularity, sphericity, and surface chemical composition and roughness on the observed behavior. This sand has a grain density (ρ_s) of 2.64 g/cm^3, a grain diameter at 10% passing (d_{10}) of 0.45 mm, a grain diameter at 50% passing (d_{50}) of 0.68 mm, and a maximum grain diameter (d_{max}) of 2.00 mm. The maximum void ratio (e_{max}) is 0.805, while the minimum (e_{min}) is 0.520. For the equivalent glass beads, ρ_s is 2.50 g/cm^3, d_{10} and d_{50} are the same as of sand, and d_{max} is 1.30 mm. Glass beads have as e_{max} of 0.679 and an e_{min} of 0.555. Figure 1 presents the sand and artificially colored droplets resting on its surface. The food colorant that makes the droplets more visible on the figure was employed only for the production of this specific photo and not at any other point in this study.

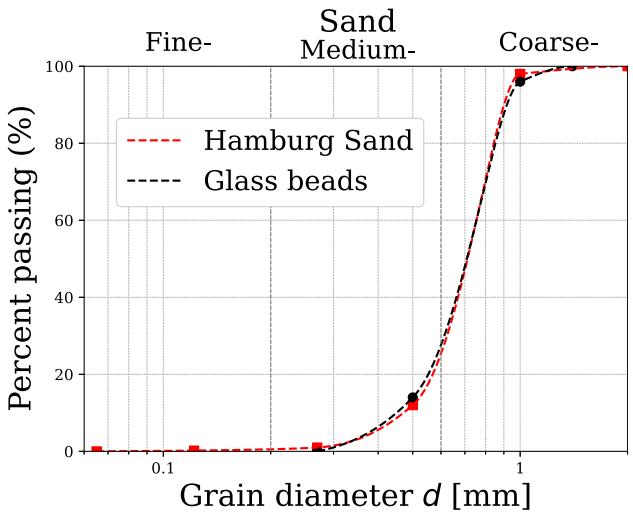

Fig. 2 Grain size distribution of Hamburger Sand and equivalent glass beads

Another characteristic that distinguishes the two chosen base materials is their thermal behavior, represented by their thermal capacity and conductivity. Although glass beads have a specific thermal conductivity of 1.129 $W/(m \cdot K)$ and a specific thermal capacity of 1.329 $kJ/(kg \cdot K)$ [39], the values for sand are around 0.250 $W/(m \cdot K)$ and 0.830 $kJ/(kg \cdot K)$, respectively [14]. Since sand has a natural origin and thus a heterogeneous composition, the values are approximated and not exact. In addition, those values represented both materials on the dry state, and they would increase in case the material was wet, as a result of the higher thermal conductivity of water.

For coating the granular materials, the cold plasma technique was used, similar to that performed in [1, 28, 37, 53]. This technique is widely used in some areas of industry, as icing control in aerospace industry [19], creation of medical devices [30], manufacturing of hydrophobic textiles [51], and manufacturing of non sticking food-related instruments [29]. In this context, [15, 41] describe other possible fluoropolymers used for surface coating and how they develop and are used in industry. To date no mention of its application for geotechnical engineering has been found by the authors, since usually the employed coating material is dimethyldichlorosilane [33]. Wax has also been employed as a coating material to induce hydrophobicity artificially in [3], and some organic compounds can as well lead to hydrophobicity naturally, normally related to forest fires or sewage contamination [13]. Because of that lack, the authors decided to coat granular materials with the fluoropolymers and study its effects. The process to coat the particles in this study consists of inserting the liquid monomer of the polymer, which for this study is the 1 H,1 H,2 H,2 H-perfluorooctylacrilate presented in Fig. 3, and the uncoated grains in a plasma chamber. The materials were air dried before this step. As a result, a monolayer of the organic polymer is deposited on the surface of the material, making it hydrophobic. All materials were coated with the same polymer.

While this approach is effective in achieving the desired hydrophobic properties, its application at an industrial scale may be limited by economic factors. In particular, the high-

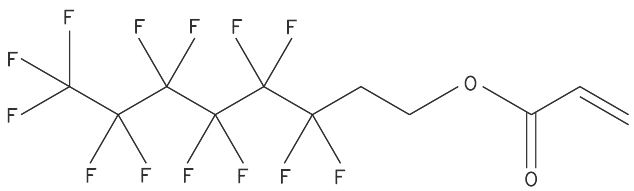

Fig. 3 1 H,1 H,2 H,2 H-perfluorooctylacrilate molecular structure

energy demand of plasma-based processing contributes significantly to overall costs. Additional concerns relate to potential environmental impacts, as the production of coating agents may result in atmospheric emissions and contamination of surface soils [10]. Moreover, when applied in situ, there is a possibility that the coating may be partially removed through interaction with groundwater [42]. Nevertheless, toxicity assessments reported by [15] suggest that per- and polyfluoroalkyl substances (PFAS) fall under the category of "polymers of low concern" (PLC) and therefore are not subject to standard polymer regulatory frameworks.

Previously to the execution of this study, the settings for the coating technique were varied and the samples produced during this process were compared in terms of hydrophobicity and durability of the applied coating. These results are described in [44]. In that study, the sand samples used for the present study are referred to as "material V7" and "material V8", while the glass beads sample is "material V5". The first sand sample was kept in the plasma chamber for 60 min without pretreatment, while the second for 20 min, after giving it an oxygen pretreatment to prepare the surface for receiving the coating. The glass beads sample was kept in the chamber for 20 min, but without the pretreatment. The index test employed for those comparisons is the water drop penetration time test, and according to the classification proposed by [6], both sand samples are extremely hydrophobic, while the glass beads sample is severely hydrophobic. Those classifications denote that droplets rested on the surface of the sand longer than 3600 s and between 600 and 3600 s on the surface of glass beads.

The contact angle of those materials was measured using the sessile drop method as proposed in [2] using a drop shape analyzer from the company KRÜSS GmbH of Hamburg, Germany. The values obtained are 113° for both sand samples and 93° for the glass beads, according to Fig. 4. However, for beads, the angle changes quite drastically in the first seconds after the droplet is placed on the sample, stabilizing at an equilibrium value of 71°. Based on the four different measurements taken for each material, the standard deviation for the sand contact angle is 2.6, while the one for glass beads is 7.5.

Figure 5 presents 2D ESEM images of PFA-C6 coated and uncoated glass beads, obtained with a Thermo Fisher Quattro microscope with a resolution of 2 *nm* owned by the Betriebseinheit Elektronenmikroskopie (BeEM) of the TUHH. Both samples were dry when the image was obtained. On them, it is noticeable that the coating is not visible, even at 250× magnification.

2.2 Raspberry Pi controlled cooling device

A cooling device controlled by a Raspberry Pi single board computer was designed and built for the experiments. It was mounted on the rotation stage of the beam line. The objective of this device was to induce water condensation on the sand grains surface via cooling of those grains and thus lowering the dew point of the air around the particles, according to the phase diagram of water, similarly to when a soda bottle is taken out of the fridge and left at room temperature for a while.

The built device is presented in Fig. 6 and consists of a sample holder, a Peltier element, a Raspberry Pi single board computer, two temperature sensors, one at the base, which also measures relative humidity, and one at the top, a DC power supply with an output of 9 volts, a heat sink and a fan, both from an old desktop computer. Thermal paste was placed between the sample holder and the Peltier element and also between the temperature sensor and the Peltier, which is visible around the thermometer in Fig. 6. The base plate, on which the pieces were mounted, was cut out of HDPE (high density Polyethylen) on a CNC machine. The diameter of the plate is 30.45 cm and its thickness is 1 cm, aiming at compatibility with the rotation stage of the beam line, as well as the placing of the screw holes. The pieces were attached to the plate with hook and loop tape and transparent adhesive tape.

The Peltier element is a small device able to induce a temperature delta between its two ceramic parallel plates, one turning hot and the other, cold, because of the Peltier effect. In the created device, the thermometer was placed on the cold side of the Peltier, and its reading was used by

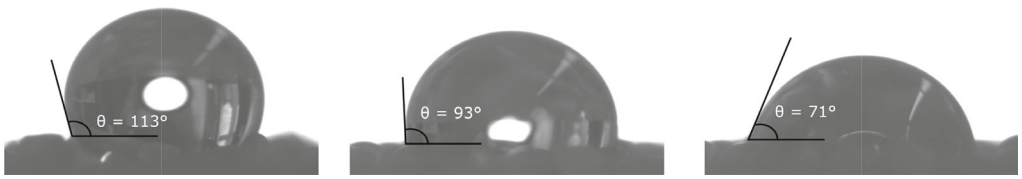

(a) V7 sand sample (b) Glass beads sample immediately after droplet is placed (c) Glass beads sample two seconds after droplet is placed

Fig. 4 Goniometer contact angle [°] measurement of PFA-C6 coated sand (**a**) and glass beads immediately after placing the droplet (**b**) and 2 s after (**c**)

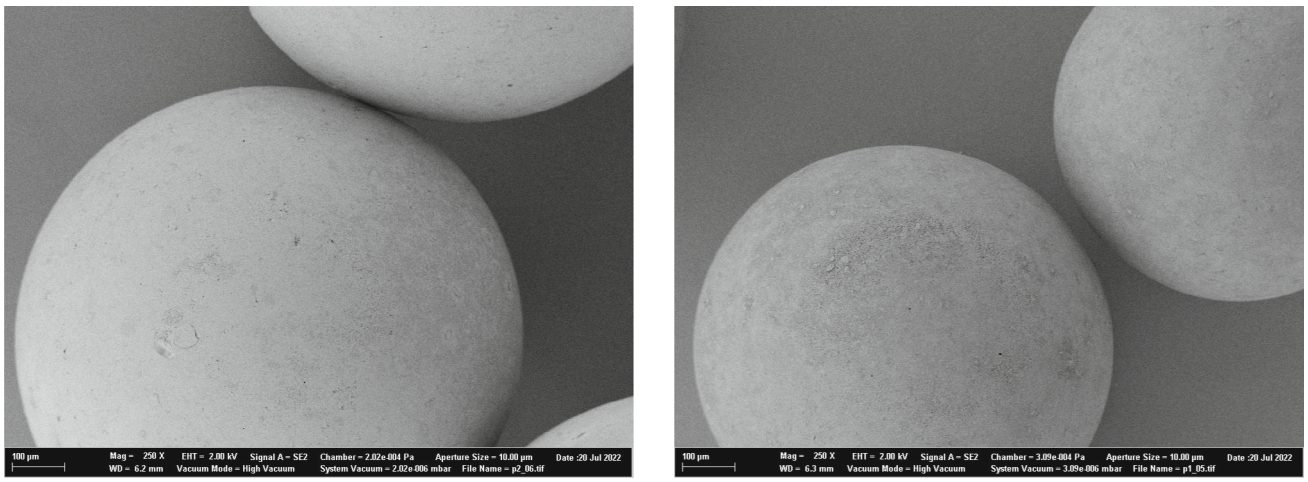

(a) PFA-C6 coated (b) Uncoated

Fig. 5 Thermo Fisher Quattro ESEM 2D images of dry PFA-C6 coated (**a**) and uncoated (**b**) glass beads. No difference can be seen between the coated and uncoated samples

the Raspberry Pi to track a target temperature by using a proportional integral derivative (PID) feedback controller.

The hot side of the Peltier was coupled with thermal paste to a heat sink, which was ventilated by a fan, in order to dissipate the heat it produced and enable the further cooling of the cold side. In order to avoid vibrations from the fan to get to the sample, this part of the system was uncoupled, meaning that the fan was not attached to the heat sink, but only to the circular base plate. The sample was mounted on the cold side of the Peltier inside a tubular sample holder made of Plexiglas with 1 cm internal diameter. In order to elevate the sample in a way that the X-ray beam would not hit the thermometer on the Peltier, a small cylinder of aluminum with compatible diameter was also inserted in the sample holder. The choice of aluminum is due to its elevated thermal conductivity. The electronic part of the final developed device was covered with small lead spheres and plates to protect against radiation before starting the imaging.

The 200-line code written in Python to read the temperature sensors and control the fan and Peltier is available on GitHub in [43]. A humidity control feature was not included in the design, although during the beam time, we realized that it could have been useful and led to finer control over the formation of the droplets.

2.3 Synchrotron computed tomography and image acquisition

The µCT imaging was conducted at the High Energy Materials Science (HEMS) Beamline P07 of PETRA III, which is located at the Deutsches Elektronen-Synchrotron (DESY) in Hamburg, Germany, and operated by Helmholtz–Zentrum Hereon. Propagation-based phase contrast tomography was performed at a sample-detector distance of 0.2 m, acquiring 5101 projections over a 180° fly-scan. The scans were carried out with a photon energy of 44 keV and an exposure time of 60 ms. Detection was achieved through an indirect detection system, utilizing a CdWO4 scintillator and a CMOS sensor-equipped camera. The raw images had dimensions of 7919 × 3000 pixels, with an effective pixel size of 0.92 µm, owing to a fivefold magnification in the optical system. For the tomographic reconstruction, filtered backprojection using a Ram-Lak filter was applied, according to the workflow outlined in the reconstruction and analysis tools for tomographic data provided by HEMS [32]. A raw binning factor of 4 was used, followed by a two-fold binning process during data processing, resulting in a final voxel size of 7.36 × 7.36 × 7.36 μm^3.

In order to analyze the formation of water droplets and the evolution of their contact angles, the temperature on the cold side of the Peltier element was fixed to 5° Celsius and sequential tomograms were obtained, each of them requiring around 10 min. Since the chamber had no humidity control feature, it was necessary to artificially increase humidity by placing a wet paper towel inside a "hat" covering the sample top. One tomogram, referred to as time step 1, was taken for the dry state of each sample, before turning the cooling device on. After that, seven tomograms were obtained of each sand and nine of the glass beads while cooling the samples. Those allowed analyzing the amount of droplets on each grain and the contact angle between those water droplets, air in the pore space, and the solid grains. Other tomograms were obtained after turning the cooling off, which are not

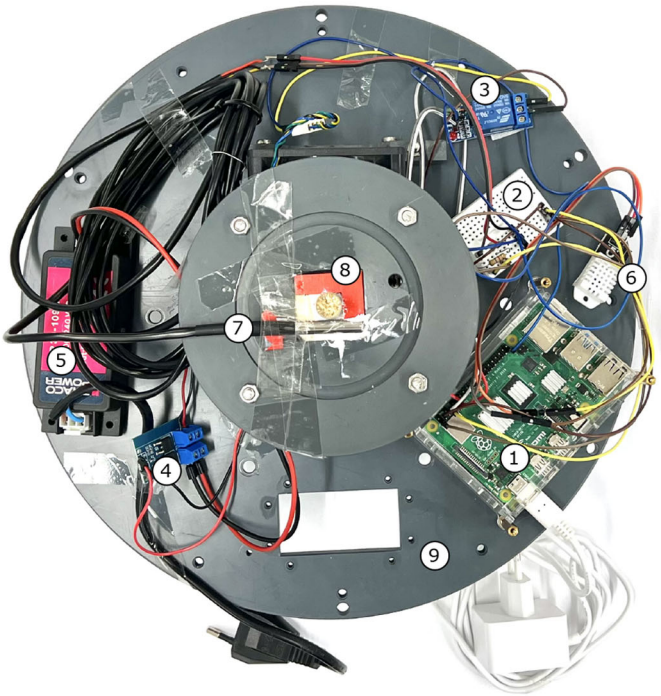

(a) Top view

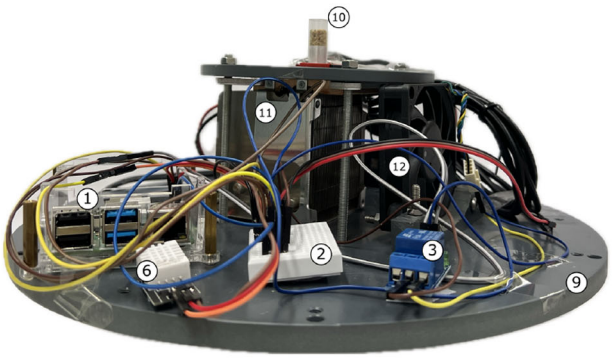

(b) Side view

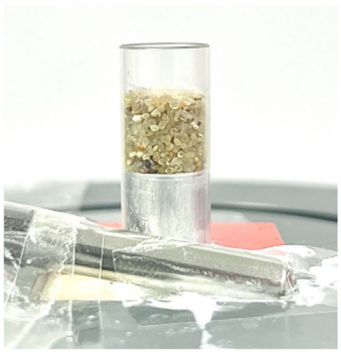

(c) Zoom on sample holder filled with sand

Fig. 6 Device created to induce water condensation on grain surface. (1) Raspberry Pi, (2) breadboard for cable and resistor connection, (3) relay module for the fan, (4) dual MOSFET switch drive module, (5) power supply, (6) DHT22 relative humidity and temperature sensor at the base, (7) DS18B20 digital temperature sensor at the Peltier, (8) 4x4 cm Peltier element (white) and plastic sample centralizing tool (red), (9) base plate, (10) sample holder + sample, (11) heat sink, and (12) fan

presented here. The whole dataset from the beam time is available in [46].

2.4 Image analysis

In order to be able to refer to the same grains in different stacks throughout the study, a first segmentation was executed, isolating only grains, which were later labeled. Given that only at some time steps there is a very small grain displacement from one tomogram to the next, it was possible to easily find these same grains on the subsequent time steps and keep referring to them by the same label value. For most time steps, no displacement is observed when a registration between them is done. Although the glass beads could rotate precisely around their center and still remain in the same position in the tomograms, the authors believe it is unlikely that this pure rotation without any translation occurs, and so this type of movement was not addressed. The labeling was executed with *spam* [40] and the MorphoLibJ extension [20] of ImageJ [36].

Figure 7 presents one slice of the tomogram, of both sand samples and glass beads, respectively, in which the labels corresponding to the grains used for the analysis in Subsect. 3.2 were superposed on the greyscale image, and are represented by a color and the number written on the grain. Only the grains that were used for the subsequent analysis in Sect. 3 have a label in Fig. 7, although all grains received a unique label in the beginning. Since for the sand samples not all grains could be found in one single slice, the slice containing the majority of them is the one presented.

To enable visualization of the relative position of these grains analyzed within the sample volume, a 2D view of the 3D representation of only the grains studied is presented in Fig. 8. The scale in the bounding box of the image is in pixels, and each pixel measures 7.36 × 7.36 μm^2.

With respect to segmentation, working with the whole image was challenging, given that the size of the droplets is very small compared to that of the grain, especially in the initial time steps. This made it almost impossible for the usual algorithms or automatic processes to segment it in its original size. The solution was to work on specific grains after separating them from the whole image by extracting a subvolume and then segmenting the three phases inside these subvolumes. For that, the Avizo software segmentation editor was used along with a watershed algorithm in this same software, which requires manual marking as a first step. Segmentation process was thus slow and laborious. Also, since every full sample scan takes around 10 min, in some cases, they are not very sharp and induce artifacts originating from droplet growing during image acquisition.

The manual counting of droplets on the selected grains followed. The contact angle of the droplets was also measured at selected droplets of the previously selected grains using the angle tool from ImageJ [36] at the 2D slices of the tomogram for each time step. The meniscus and water clusters that formed involving those particles were also analyzed. These results are presented in Subsect.3.2.

3 Results and discussion

As stated in Sect. 1, this paper aims to describe the wetting mechanism of hydrophobic granular material through water-vapor condensation. This is done in two stages: the first one is concerned with the formation, growth, and coalescence of the liquid water droplets on the surface of a single grain and the second regards the formation of a water bridge between two or more grains.

3.1 ESEM findings: 2D analysis

Figures 9 and 10 present 2D environmental scanning electron microscope (ESEM) images of the wetting of the hydrophobic and hydrophilic Hamburg Sand, respectively, obtained with a Thermo Fisher Quattro, an electronic microscope able to regulate relative humidity inside its sample chamber by changing pressure and temperature. By increasing the relative humidity and lowering the temperature, water condensates on the surface of the material. The gaseous secondary electron detector was employed, along a beam voltage of 15 kV. In Figs. 9 and 10, the mechanism of wetting hydrophobic granular material via water droplet condensation is clear, but only qualitatively. It is noticeable

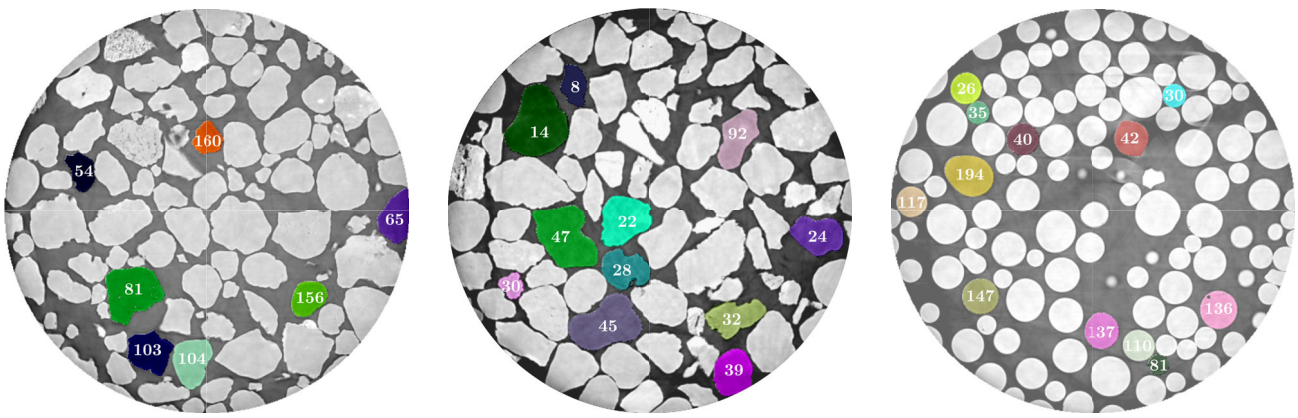

(a) V7 Sand, slice 8 of 360, showing 7 of the 12 grains on which the analysis is based

(b) V8 Sand, slice 30 of 360, showing 11 of the 12 grains on which the analysis is based

(c) Glass beads, slice 6 of 360, showing all the 12 grains on which the analysis is based

Fig. 7 Superposition of labeled image and greyscale CT slice. Only the labels of grains used for the analysis in section 3.2 are presented, but not all of them are shown, since this is a 2D slice of a 3D tomogram

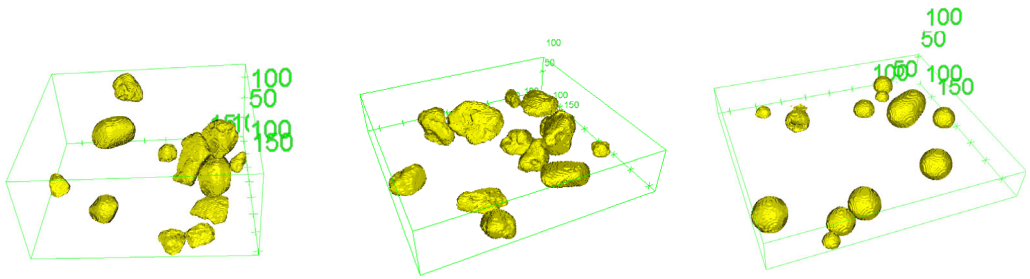

(a) V7 Sand (b) V8 Sand (c) Glass beads

Fig. 8 3D visualization of the labeled grains that were used for the analysis inside of the volume of the samples

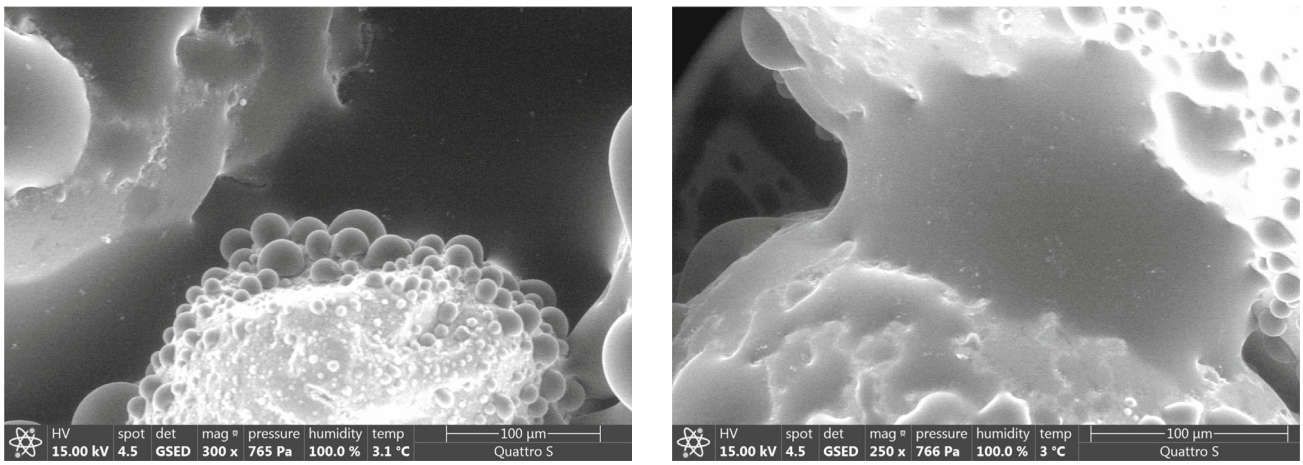

(a) Development of water droplets. (b) Development of meniscus between grains.

Fig. 9 2D ESEM images of wetting via water condensation of hydrophobic sand

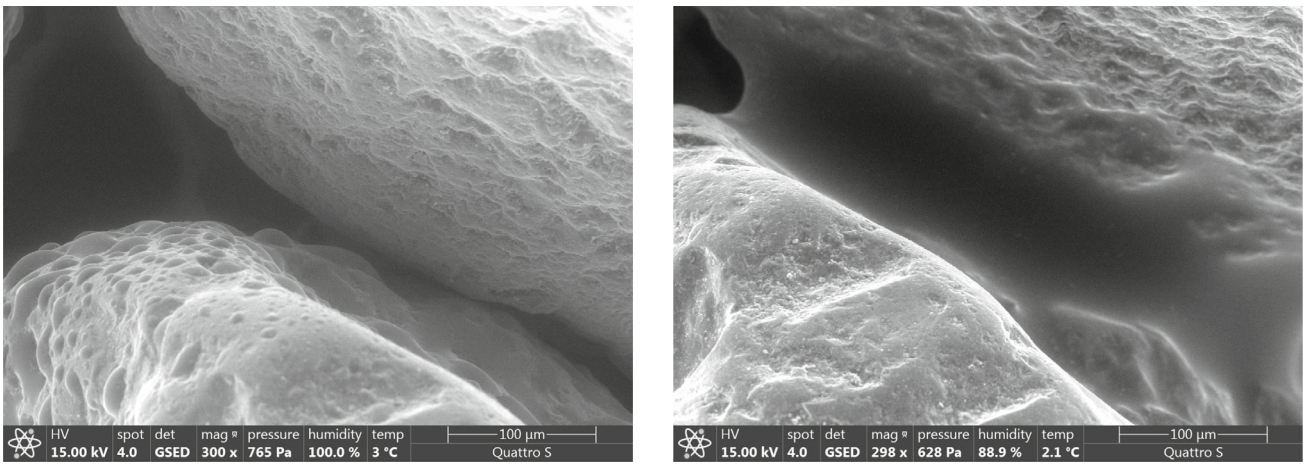

(a) Development of water droplets. (b) Development of meniscus between grains.

Fig. 10 2D ESEM images of wetting via water condensation of hydrophilic sand

that at first small water droplets with contact angles larger than 90° form and, as they grow in volume as more water condenses and they coalesce, their contact angle becomes progressively smaller and, eventually, smaller than 90°. For the hydrophilic counterpart in Fig. 10, the formation of the droplets is not very expressive and, where visible, the contact angle is apparently smaller than 90°.

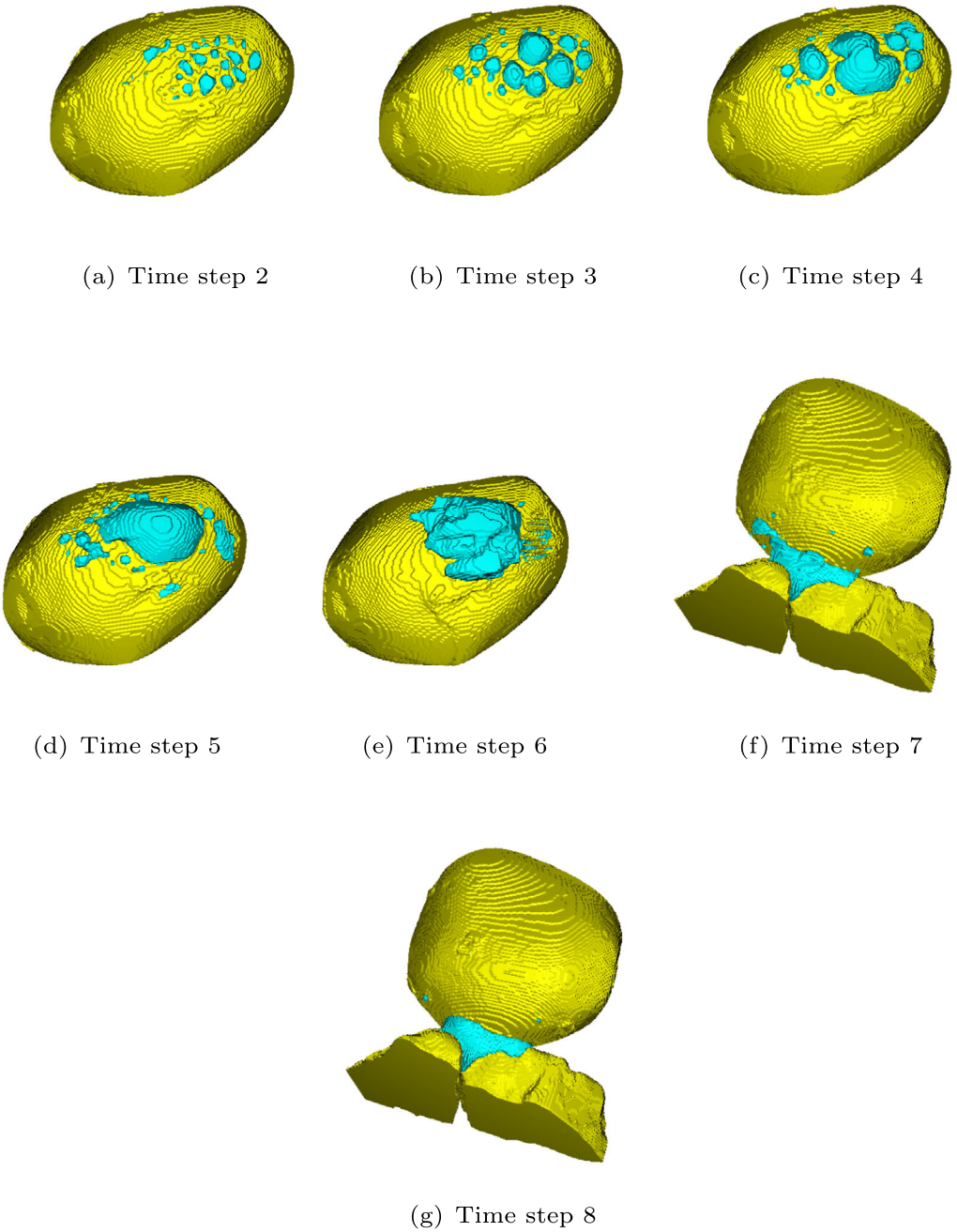

Fig. 11 Three phase (grain, water, and background) segmentation of a single V7 sand grain (label 672) and the water around it at the subsequent 8 time steps. All grains are shown from the same perspective, but on subfigures (**f**) and (**g**), in which it was rotated so that the grains it connects to would not prevent the view of the meniscus. The biggest dimension of the presented grain is 1.15 mm, and the time step from one subfigure to the next is around 10 min

Regarding the meniscus, when the hydrophobic grain connects to its neighbor in Fig. 9b, the meniscus observed between them is apparently concave, similarly to the hydrophilic sample in Fig. 10b, which characterizes hydrophilic behavior. The contact angle of the meniscus between the hydrophobic grains appears to be larger than the one between the hydrophilic grains, although both seem to be smaller than 90°. Since Laplace pressure is dependent on radial and azimuthal radius, it is impossible to say whether the suction is positive or negative.

Although condensation of water droplets on the hydrophobic surface was already investigated using an environmental scanning electronic microscope (ESEM) in [17, 18, 45], the phenomenon was not investigated with a technique that produces 3D images. Given that the ESEM is only able to provide 2D images, it is not possible to

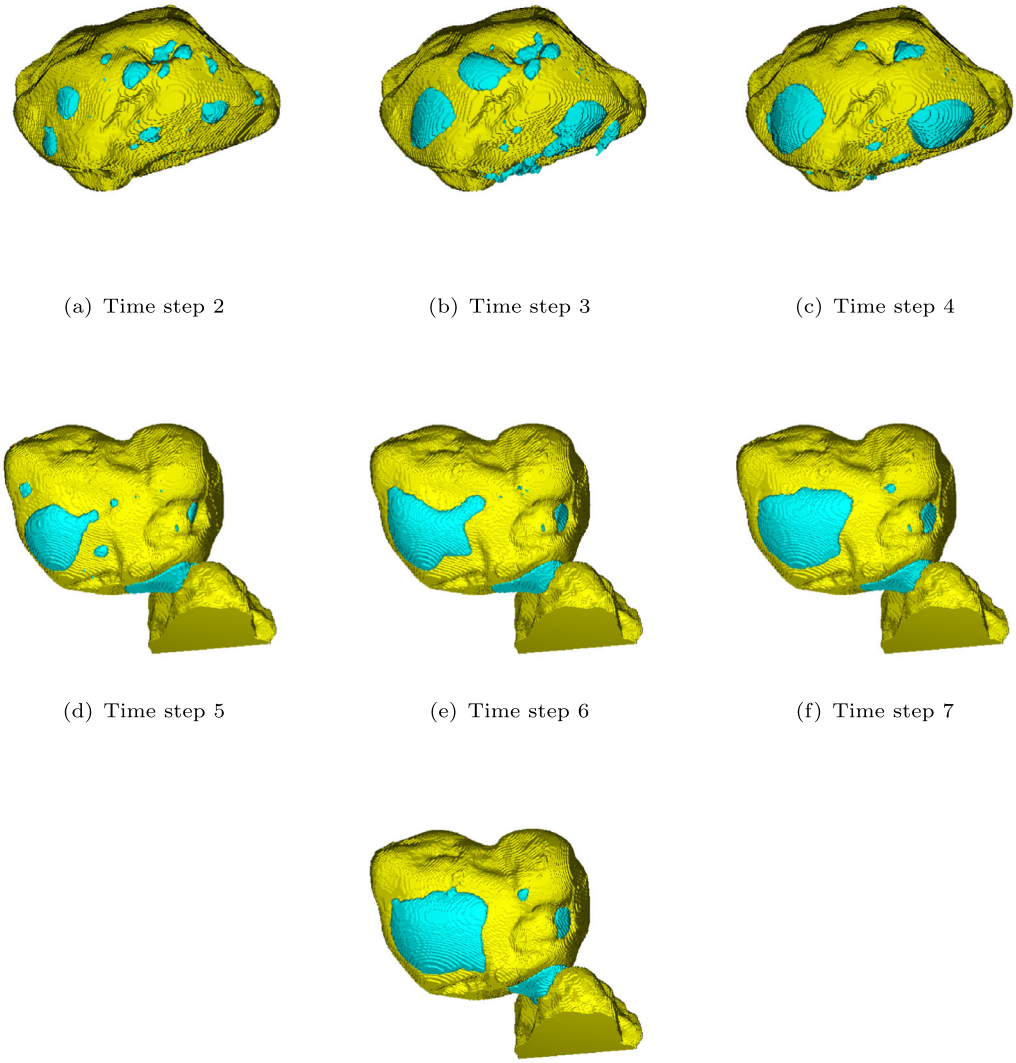

(a) Time step 2 (b) Time step 3 (c) Time step 4

(d) Time step 5 (e) Time step 6 (f) Time step 7

(g) Time step 8

Fig. 12 Three phase (grain, water, and background) segmentation of a single V8 sand grain (label 47) and the water around it at the subsequent 8 time steps. Grains are shown from the same perspective on Subfigs. (**a**–**c**) and then again from Subfig. (**d**–**g**), in which it was rotated so that the grains it connects to would not prevent the view of the meniscus. The biggest dimension of the presented grain is 1.07 mm, and the time step from one subfigure to the next is around 10 min

count droplets or measure their contact angles. This creates the necessity of a 3D analysis, using a method that enables the quantitative analysis.

3.2 CT findings: 3D analysis

3.2.1 Droplet formation

Figures 11, 12 and 13 present each a single particle of each analyzed hydrophobic material for all different consecutive time steps. The label of the sand grain depicted in Fig. 11 is 672, the one in Fig. 12 is 47, and the one for the glass bead in Fig. 13 is 110, according to the values presented in Fig. 7. Water is presented in blue and solids in yellow. The visualization presented was created using the 3D Suite [34] of ImageJ. It is noticeable that for all particles the droplets are concentrated on one side of its surface. This is the top of the particles, closer to the moist paper placed on top of the samples to increase relative humidity. In addition, for all three materials, the first time step is not shown, because it only shows the dry particle before the cooling system is switched on.

Qualitatively, regarding the V7 sand grain, one can notice that from time step two in Fig. 11a to step six in Fig. 11e, the droplets coalesce and increase in volume, creating one larger water body that later connects to the

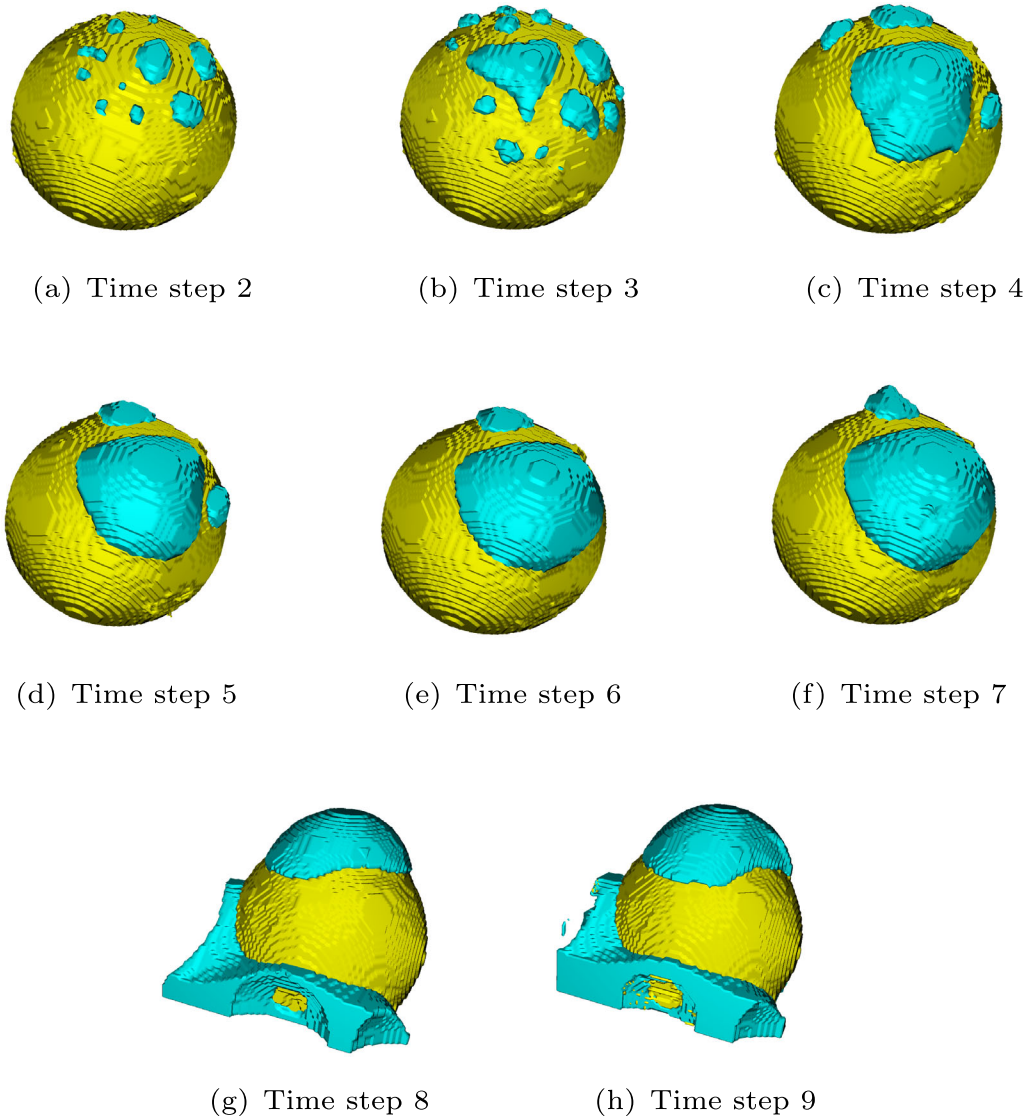

Fig. 13 Three phase (grain, water, and background) segmentation of a single glass bead (label 110) and the water around it at the subsequent 9 time steps. The grain was rotated from subfigure (**f**–**g**) and kept at the same position everywhere else in order to facilitate viewing of the water at its base. The diameter of the presented bead is 0.52 mm, and the time step from one subfigure to the next is around 10 min

neighboring grain between Fig. 11e and f. A very similar process is also observed on the V8 sand sample and on the glass beads, presented in Figs. 12 and 13, although initially fewer droplets are present.

For a quantitative understanding of the process, the amount of droplets and their contact angles, both at each imaged time step, were obtained and plotted in Figs. 14 and 15. The identification number of each grain still corresponds to the labels presented in Fig. 7.

The plots presented in Figs. 14 and 15 confirm the observations from the preliminary studies described in the introduction and also the inferences from the qualitative 2D analysis. The averaged amount of droplets for all studied grains, indicated by the solid red lines in Fig. 14, starts at higher values and monotonically decreases. Although the tendency is the same for all materials, less droplets condensate on the surface of the V8 sand (Fig. 14b) at the beginning, around half of the amount measured on the V7 sand (Fig. 14a). Although they both consist of the same base material, the second is left for a longer time in the coating chamber, as described in Subsect. 2.1, which then makes it a more hydrophobic material in terms of persistency, even though they have the same contact angle as described in Subsect. 2.1. When comparing the V8 sand and the glass beads (Fig. 14c), which are kept in the coating chamber for the same time, the initial amount of droplets is almost the same. This reinforces the conclusion that more droplets tend to form on the surface of materials

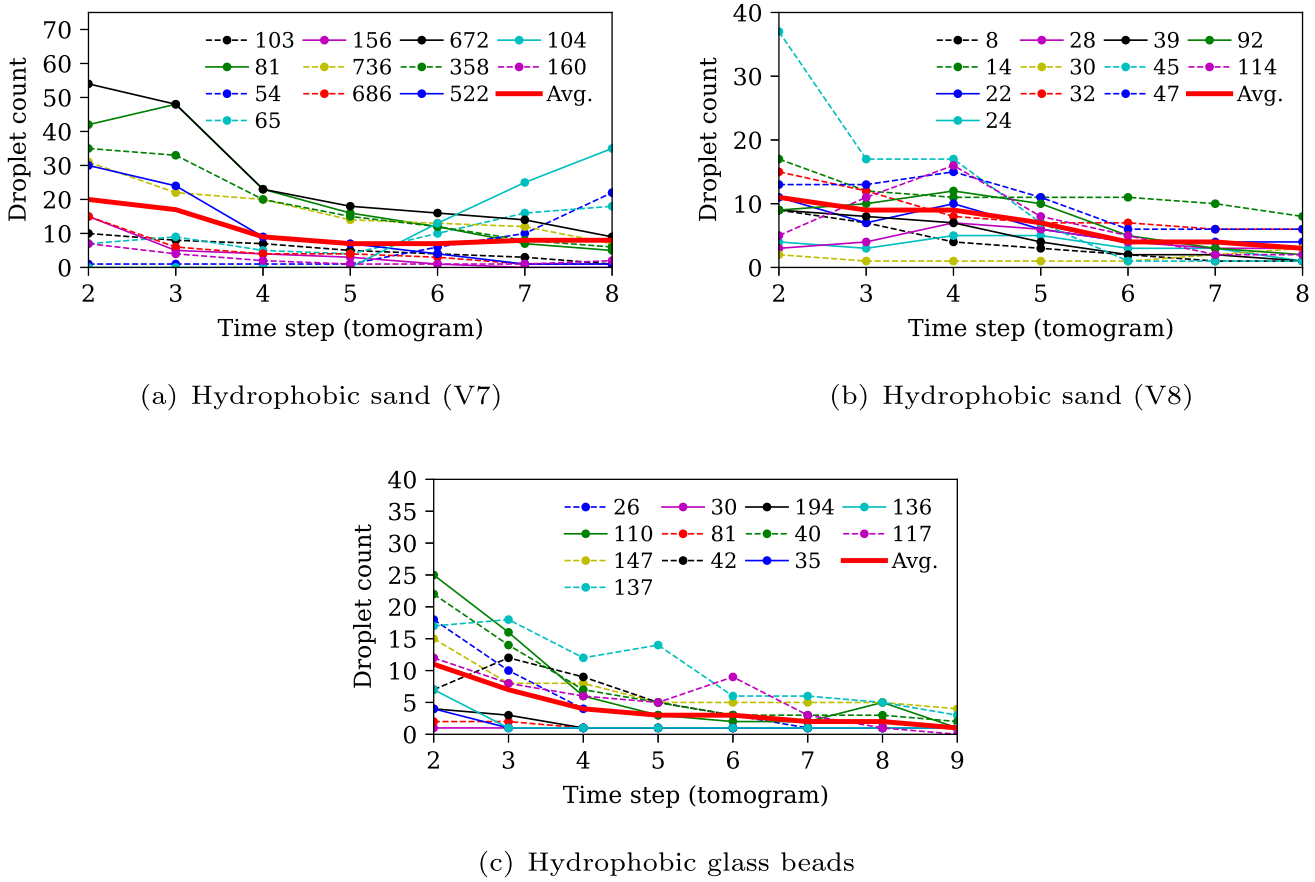

(a) Hydrophobic sand (V7)

(b) Hydrophobic sand (V8)

(c) Hydrophobic glass beads

Fig. 14 Evolution of the amount of droplets (y-axis) present on the surface of specific grains, described by their label value from Fig. 7, during time (x axis)

are more persistently hydrophobic when they are wet via water condensation.

Regarding contact angles (CA), of which the average value is shown by the solid red lines in Fig. 15, the initial value is larger than 90° for V7 sand and glass beads, depicting their hydrophobic behavior in terms of the classic definition. V8 sand, presented in Fig. 15b, induces the condensation of droplets that have a CA smaller than 90° already at the beginning. This is then no classical hydrophobic behavior, but the data still agree with the trend observed for the other samples and the contact angle is still much higher than the original value for uncoated sand, which is around 30°, even though it is not larger than 90°. After the initial time step, CA of the V8 sand monotonically decreases over time for all samples while droplets coalesce and increase in volume, until they reach a final CA value around 40°, closer to that of uncoated sand. This result is compatible with the differences in coating time each sample was subjected to, as described in Subsect. 2.1. While the V8 sand was kept in the chamber for 20 min after oxygen pretreatment, the V7 sand was kept for 60 min, 3 times longer, which made it more hydrophobic. Although contact angle has been shown to be time dependent [50, 52], the time spans investigated in these studies are usually much longer than the one used here. Also, in this paper, there is an ongoing condensation of liquid water on the materials surface, which is then assumed to be the leading mechanism affecting the contact angle. Because of that, the time dependency is not approached in detail.

3.2.2 Water bridges connecting grains

The second stage of the analysis focuses on the grains connecting to their neighbors via water bridges. 26 of the 36 evaluated grains connected with their neighbors, considering both sand samples and glass beads. For most of them, two grains connected first and then these menisci connected to a grown droplet from a third grain. There is no statistical significance relating sample composition and bridge development. Over time, during the last third of the total test time span, larger water clusters were formed

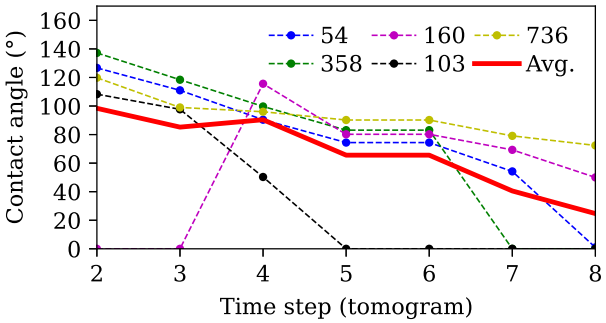

(a) Hydrophobic sand (V7)

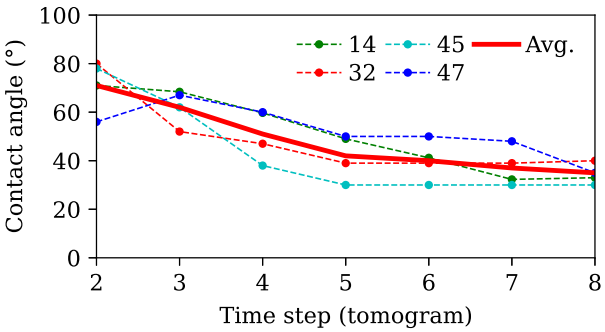

(b) Hydrophobic sand (V8)

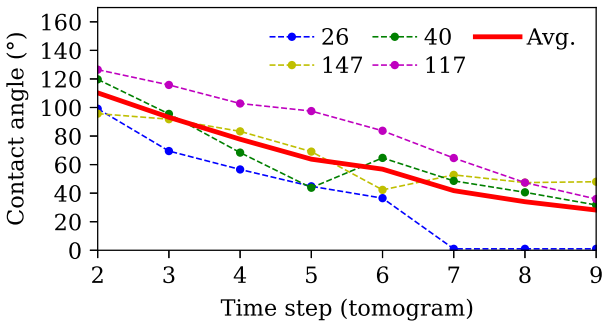

(c) Hydrophobic glass beads

Fig. 15 Evolution of the droplet contact angle (y-axis) with time (x-axis) on specific grains, described by their label value from Fig. 7. Step 1 is not presented since there are not droplets and thus, their contact angle is not measured

connecting the cooling plate at the bottom of the sample and some of the grains closer to it. As those greater clusters start saturating the sample from the bottle, the CT imaging was interrupted, since the focus of this study is the condensed droplets and subsequently developed menisci.

Grains that connected to two or more neighbors for two or more time steps were selected for the bridge contact angle analysis. The angle was again measured using the ImageJ [36] angle tool on the 2D slices of the tomogram. Although the values present high variability, the contact angle between these water structures and the glass beads and sand grains averages around 60°. For glass beads, a contact angle of 60° is compatible with the value presented in Fig. 4c. While the small droplets at the beginning of the wetting process occur with CA values of around 120°, according to the plot in Fig. 15c, this angle drops closer to the equilibrium value measured by the goniometer as the droplets coalesce and join to form a meniscus at the end of the wetting process. For the sand counterpart, the droplets at the beginning of the process have contact angles compatible with the 113° measured by the goniometer and presented in Fig. 4a, which also progressively decrease, reaching a similar final value. Even though the analysis in this study is focused on contact angle, it is important to remember that for a small bridge, the contact line and the available liquid volume are also crucial for its shape.

According to the literature review presented in Sect. 1, it could be expected that the coated particles would still behave as hydrophobic in the pendular and funicular regimens and form convex menisci until achieving a higher local saturation degree and amount of liquid water in contact with them. Nevertheless, the obtained average contact angle values for sand and glass beads is around 60°, which is smaller than the 90° threshold and thus characterize hydrophilic behavior according to the microscopic criterion. The explanation for this observed behavior could be that as the condensed water droplets multiply, coalesce, and grow in volume, they tend to form a thin water film spread on the surface of the particle, and then, this film dictates the properties of the interaction between the water in the meniscus and the other solid particles. However, this film is not seen in the CT data (Figs. 11, 12 and 13), only in the 2D ESEM images presented in Fig. 9. In them, the mentioned film is being formed around the grain from the coalescing droplets, especially visible in Fig. 9b.

3.2.3 Further inferences

Comparing the analyzed behavior of hydrophobic sand and glass beads, no significant difference is observed. On both small droplets with higher contact angles condense, and then coalesce to form larger droplets with lower contact angles, which in turn can connect to a neighbor and form a meniscus with a contact angle that indicates hydrophilic tendency. This shows that the overall behavior is general for particle media and probably not related to peculiarities of the grain, like shape, angularity, texture, or thermal behavior. To make it a statement, however, those effects would need to be investigated individually in samples prepared with this aim, which was not performed in this study.

4 Conclusion

This paper investigates the wetting of hydrophobic material via water droplet condensations by means of electronic microscopy and synchrotron computed tomography. Sand and glass beads with similar grain size distribution were made hydrophobic via cold plasma polymerization, which coated them with a PFA-C6 monolayer not visible by ESEM. An in situ Peltier based miniature cooling device controlled by a Raspberry Pi was designed to induce droplet condensation on the material's surface during CT scanning.

Although hydrophobic behavior and doubly convex menisci were expected in the pendular and funicular regimes, the contact angles of these water structures were closer to 60°, indicating hydrophilicity. Contact angles above 90° were observed only at the beginning, while small droplets condensed on the material's surface and coalesced between themselves. Similarly to wetting via water inflow the hydrophobicity is lost after a specific degree of local saturation, although the mechanism controlling both wetting processes is different, as described in Subsect.3.2. Unlike previous studies that made qualitative statements based on 2D imaging techniques in which it is not possible to count droplets or measure contact angles, this study employs CT imaging, which provides qualitative inferences.

Unfortunately, the observations point in an unfavorable direction for the general applications of this type of hydrophobic materials on the macroscale for higher local saturation degrees, given their low efficiency in repelling water in and after the funicular state. The properties could be tuned for specific application involving less condensation and lower saturation degrees, however. The technique's economical viability at large scale is also discouraging, given the high-energy demand for coating the particles, as described in Subsect. 2.1.

For future research, a humidity control feature should be added to the created device, enhancing the control over the relative humidity inside the sample and thus over the formation of the droplets, menisci, and clusters. Other coating technologies could also be investigated, focusing in particular on the eco-friendliness of the substance.

Acknowledgements The authors acknowledge the funding of this research by the German Research Foundation (Deutsche Forschungsgemeinschaft, DFG) in the framework of Research Training Group GRK 2462: Processes in natural and technical Particle-Fluid-Systems at Hamburg University of Technology (TUHH). We acknowledge the Deutsches Elektronen-Synchrotron DESY (Hamburg, Germany), a member of the Helmholtz Association HGF, for the provision of experimental facilities. Parts of this research were carried out at PETRA III. Beamtime was allocated for proposal 20220840. This research was supported in part through the Maxwell computational resources operated at DESY and by the project Holistic Data Analysis (HoliDAy) of the Innovation-, Information-& Biologisation-Fonds (I2B) of Hereon. The authors would also like to thank the Betriebseinheit Elektronenmikroskopie (BeEM) at the TUHH and Mattia Gianini, PhD, from Thermo Fisher for the ESEM analysis. In a addition, we would like to thank our former bachelor students Ahmad Jbayer and Omer Alrefai for their contribution to this work, especially in relation to obtaining the amount of droplets in the particles and their contact angles. Sneha George, our former intern, is also to be thanked for her help with segmenting greyscale CT images.

Funding Open Access funding enabled and organized by Projekt DEAL.

References

1. Ahmad D, Van Den Boogaert I, Miller J et al (2018) Hydrophilic and hydrophobic materials and their applications. Energy Sources Part A Recover Util Environ Eff 40(22):2686–2725
2. Bachmann J, Horton R, Van Der Ploeg R et al (2000) Modified sessile drop method for assessing initial soil-water contact angle of sandy soil. Soil Sci Soc Am J 64(2):564–567
3. Bardet JP, Jesmani M, Jabbari N (2014) Permeability and compressibility of wax-coated sands. Géotechnique 64(5):341–350
4. Bayad M, Chau HW, Trolove S et al (2020) The relationship between soil moisture and soil water repellency persistence in hydrophobic soils. Water 12(9):2322

5. Beckett C, Fourie A, Toll D (2016) Water repellent soils: the case for unsaturated soil mechanics. In: 3rd European Conference on Unsaturated Soils: E-UNSAT 2016. EDP Sciences, p 11011
6. Bisdom E, Dekker L, Schoute JT (1993) Water repellency of sieve fractions from sandy soils and relationships with organic material and soil structure. In: Soil structure/soil biota interrelationships. Elsevier, p 105–118
7. Chau T (2009) A review of techniques for measurement of contact angles and their applicability on mineral surfaces. Miner Eng 22(3):213–219
8. Clothier B, Vogeler I, Magesan G (2000) The breakdown of water repellency and solute transport through a hydrophobic soil. J Hydrol 231:255–264
9. Czachor H, Doerr S, Lichner L (2010) Water retention of repellent and subcritical repellent soils: new insights from model and experimental investigations. J Hydrol 380(1–2):104–111
10. Dauchy X (2023) Evidence of large-scale deposition of airborne emissions of per-and polyfluoroalkyl substances (pfass) near a fluoropolymer production plant in an urban area. Chemosphere 337:139407
11. DeBano LF (2000) Water repellency in soils: a historical overview. J Hydrol 231:4–32
12. Doerr SH (1998) On standardizing the 'water drop penetration time'and the 'molarity of an ethanol droplet'techniques to classify soil hydrophobicity: a case study using medium textured soils. Earth Surf Proc Landf J Br Geomorphol Group 23(7):663–668
13. Doerr SH, Shakesby R, Walsh R (2000) Soil water repellency: its causes, characteristics and hydro-geomorphological significance. Earth Sci Rev 51(1–4):33–65
14. Farouki OT (1981) Thermal properties of soils. Tech. rep
15. Henry BJ, Carlin JP, Hammerschmidt JA et al (2018) A critical review of the application of polymer of low concern and regulatory criteria to fluoropolymers. Integr Environ Assess Manag 14(3):316–334
16. Kammerhofer J, Fries L, Dupas J et al (2018) Impact of hydrophobic surfaces on capillary wetting. Powder Technol 328:367–374
17. Karatza Z, Buckman J, Medero GM, et al. (2020) Effect of wetting and drying on meniscus structures in hydrophobic sands. In: E3S Web of Conferences. EDP Sciences, p 03040
18. Karatza Z, Buckman J, Medero GM et al (2021) Evolution of meniscus structures in hydrophobic granular systems. J Hydrol 603:126954
19. Keley MM (2017) Super-hydrophobic surfaces based on fluorinated carbon and its application on avoiding ice-accretion. PhD thesis, Universidade Federal do Rio de Janeiro
20. Legland D, Arganda-Carreras I, Andrey P (2016) MorphoLibJ: integrated library and plugins for mathematical morphology with ImageJ. Bioinformatics 32(22):3532–3534. https://doi.org/10.1093/bioinformatics/btw413
21. Letey J (1969) Measurement of contact angle, water drop penetration time and critical surface tension
22. Likos WJ, Lu N (2004) Hysteresis of capillary stress in unsaturated granular soil. J Eng Mech 130(6):646–655
23. Lin H, Lourenço SD (2022) Accelerated weathering of hydrophobized sands. Acta Geotech 17(2):377–390
24. Lin H, Huang G, Lourenço SD et al (2024) An exploration on the degradation of hydrophobized sands as a subgrade impervious barrier during one-year outdoor weathering. Acta Geotech 19:1–15
25. Lourenço S, Gallipoli D, Augarde CE et al (2012) Formation and evolution of water menisci in unsaturated granular media. Géotechnique 62(3):193–199
26. Lourenço S, Saulick Y, Zheng S et al (2018) Soil wettability in ground engineering: fundamentals, methods, and applications. Acta Geotech 13:1–14
27. Lourenço SD, Wang GH, Kamai T (2015) Processes in model slopes made of mixtures of wettable and water repellent sand: implications for the initiation of debris flows in dry slopes. Eng Geol 196:47–58
28. Maciejewski H, Karasiewicz J, Dutkiewicz M et al (2015) Hydrophobic materials based on fluorocarbofunctional spherosilicates. SILICON 7(2):201–209. https://doi.org/10.1007/s12633-014-9264-5
29. Magens OM, Liu Y, Hofmans JF et al (2017) Adhesion and cleaning of foods with complex structure: effect of oil content and fluoropolymer coating characteristics on the detachment of cake from baking surfaces. J Food Eng 197:48–59
30. Matsuoka Y, Iida O, Suemitsu K et al (2021) Use of a fluoropolymer-based paclitaxel-eluting stent for arteriovenous graft outflow vein stenosis in hemodialysis patients. J Vasc Surg Cases Innov Tech 7(2):326–331
31. McHale G, Newton M, Shirtcliffe N (2005) Water-repellent soil and its relationship to granularity, surface roughness and hydrophobicity: a materials science view. Eur J Soil Sci 56(4):445–452
32. Moosmann J, Ershov A, Weinhardt V et al (2014) Time-lapse X-ray phase-contrast microtomography for in vivo imaging and analysis of morphogenesis. Nat Protoc 9(2):294–304. https://doi.org/10.1038/nprot.2014.033
33. Ng S, Lourenço S (2016) Conditions to induce water repellency in soils with dimethyldichlorosilane. Géotechnique 66(5):441–444
34. Ollion J, Cochennec J, Loll F et al (2013) Tango: a generic tool for high-throughput 3d image analysis for studying nuclear organization. Bioinformatics 29(14):1840–1841
35. Quéré D, Lafuma A, Bico J (2003) Slippy and sticky microtextured solids. Nanotechnology 14(10):1109
36. Schindelin J, Arganda-Carreras I, Frise E et al (2012) Fiji: an open-source platform for biological-image analysis. Nat Methods 9(7):676–682. https://doi.org/10.1038/nmeth.2019
37. Schroeter B, Jung I, Bauer K et al (2021) Hydrophobic modification of biopolymer aerogels by cold plasma coating. Polymers 13(17):3000
38. Shahraeeni E, Or D (2012) Pore-scale evaporation-condensation dynamics resolved by synchrotron x-ray tomography. Phys Rev E-Stat Nonlinear Soft Matter Phys 85(1):016317
39. Sigmund Lindner GmbH (2019) SiLibeads glass beads type S: product data sheet. Tech. Rep. V5/2019. Sigmund Lindner GmbH, Warmensteinach, Germany, https://www.sili.eu/wp-content/uploads/2018/08/SiLibeads_Type_S-1.pdf, originally created 2017–04-06, updated 2019–03-04
40. Stamati O, Andò E, Roubin E et al (2020) spam: software for practical analysis of materials. J Open Source Soft 5:2286. https://doi.org/10.21105/joss.02286
41. Teng H (2012) Overview of the development of the fluoropolymer industry. Appl Sci 2(2):496–512
42. Thepaksorn P, Lee P, Shiwaku Y, et al. (2023) Formation and degradability of per-and polyfluoroalkyl substances in river soils around a fluoropolymer-manufacturing plant in Osaka. Japan, pp 1–9
43. Toffoli CM (2023) Sauna_Pi Python code. https://github.com/ctoffolituhh/sauna_pi/tree/main/
44. Toffoli CM, Milatz M, Grabe J (2023) On the resistance of hydrophobic soil polymer coatings created by cold plasma polymerization. E3S Web of Conferences 382:18003. https://doi.org/10.1051/e3sconf/202338218003. https://www.e3s-conferences.org/articles/e3sconf/abs/2023/19/e3sconf_unsat2023_18003/e3sconf_unsat2023_18003.html. EDP Sciences

45. Toffoli CM, Milatz M, Grabe J (2024) Investigation of coated hydrophobic granular materials by means of computed tomography and environmental scanning electron microscopy. In: E3S Web of Conferences. EDP Sciences
46. Toffoli CM, Milatz M, Moosmann J, et al. (2024) Synchrotron ct images of hydrophobic sand: 1. wetting via droplet condensation and 2. water drop penetration time test. https://doi.org/10.15480/882.8774
47. Toffoli CM, Milatz M, Moosmann JP, et al. (2025) Synchrotron-radiation computed tomography of the water drop penetration time test on hydrophobic soils. J Rock Mech Geotech Eng
48. Vogel J, Balshaw H, Doerr S et al (2020) Measuring water repellency of individual particles: the new "micro-wilhelmy plate method'' and its applicability to soil. Geoderma 371:114384
49. Vogelmann E, Reichert J, Prevedello J et al (2013) Threshold water content beyond which hydrophobic soils become hydrophilic: the role of soil texture and organic matter content. Geoderma 209:177–187
50. Wang Z, Wallach R (2020) Effects of time-dependent contact angle on wettability of subcritically water-repellent soils. Water Resour Res 56(10):e2020WR027314
51. Yang B, Jiang S, Huang J, et al. (2023) Applications of fluoropolymer nanocomposites in textile industry. In: Advanced Fluoropolymer Nanocomposites. Elsevier, p 719–754
52. Yiannos PN (1962) Molecular reorientation of some fatty acids when in contact with water. J Colloid Sci 17(4):334–347
53. Zainal MNF, Redzuan N, Misnal MFI (2015) Brief review: cold plasma. Jurnal Teknologi 74(10)
54. Zhou Z, Leung AK (2022) Modifying the mechanical properties of sand by using different hydrophobic conditions. Acta Geotech 17(9):3783–3797